19

Vibration Analysis of a Moving Probe with Long Cable for Defect Detection of Helical Tubes

Takumi Inoue and Atsuo Sueoka
Department of Mechanical Engineering, Kyushu University
Japan

1. Introduction

A defect detection of a heating tube installed in a power station is a very important process for avoidance of a serious disaster. The defect detection for the fast breeder reactor "Monju" in Japan is implemented by feeding an eddy current testing (ECT) probe (Isobe et al., 1995; Robinson, 1998) with a magnetic sensor, into the tube. The ECT probe (hereafter, simply called probe) is controlled so as to move in the heating tube at a constant velocity. A peculiar feature of the heating tubes in "Monju" is that each tube is mostly helical. An undesirable vibration of the probe always happened in the helical heating tube under a certain condition (Inoue et al., 2007). The vibration was considerably large and generated an obstructive noise in the signal of the magnetic sensor. It made the detection of defects difficult. Some papers reported similar problems (Bihan, 2002; Giguere et al., 2001; Tian and Sophian, 2005), but a large vibration of the probe was not involved. A key to the problem is that the noise in the signal was accompanied with the hard vibration. Several characteristics of the vibration became clear through some experiments by using a mock-up, and a countermeasure was taken by making use of the characteristics of the vibration (Inoue et al., 2007). However, an essential factor on the cause of the vibration was still unclear. Since the noise in the signal is highly correlated with the vibration, a thorough investigation of the vibration is needed. It is desirable to find out the cause of the vibration in order to remove or reduce the vibration and ensure the reliability of the inspection.

In this study, the cause of the vibration is assumed to be Coulomb friction between floats, which are attached to the probe, and the inner wall of the heating tube on the basis of the experimental results. An analytical model is obtained by taking Coulomb friction into account and numerical simulation is implemented by applying a step-by-step time integration scheme. However, the analytical model has a very large number of degree of freedom. Furthermore, there are many points on which Coulomb friction acts when the probe is fed into the tube under air pressure since many floats, which are in contact with the inner wall of the heating tube, are attached to the probe. It implies that a lot of strong non-linearities exist in the analytical model. There is no precedent for this kind of problem, and heavy computational costs are ordinarily required to carry out the numerical simulation.

Sueoka et al. (1985) presented the Transfer Influence Coefficient Method (Inoue et al., 1997; Kondou et al., 1989, hereafter: TICM), which is a computational method for a dynamic

response of a structure and has advantages in computational accuracy and speed. The TICM is especially good at a longitudinally extended structure, such as a pipeline system and rotational machinery of a large plant. The advantages of the TICM are outstanding in an application to such structures. The probe can be regarded as a long cable, so that it exactly coincides with the structure suitable for the TICM. The TICM is applicable to various fields of the dynamic response, that is, free vibration analysis, forced vibration analysis, and time historical response analysis. The numerical simulation of the probe is efficiently implemented by applying the time historical response analysis of the TICM. The results of the numerical simulation qualitatively agree well with the experimental results. It confirms the validity of the assumption that the vibration is caused by Coulomb friction. In other words, the numerical simulation is regarded as an available tool to estimate a vibration of some modified probes. Based on this study, some improvements of probe sufficiently suppress the vibration, and a reliable inspection of helical tubes is realized.

2. The mock-up experimental equipment and analytical model of the probe

A mock-up experimental equipment is shown in Fig. 1. For the most part, the heating tube is helical. Six heating tubes with different helical diameters are mounted in the mock-up. The probe consists of a remote field (RF) sensor, cable and floats as shown in Fig. 2. The floats are attached to the cable at equal spaces. The probe is fed into the heating tube from the upper side of the steam generator. The RF sensor inspects the attenuation of the wall thickness of the heating tube by detecting the change of eddy current. The cable of the forward section from the sensor is called the guide cable and the aft section is called the carrier cable. A drag force which acts on the floats by means of dry compressed air flow is the driving force of the probe. The directions of the air flow and the movement of the probe are the same, that is, the direction of the air flow in the insertion process is opposite to the

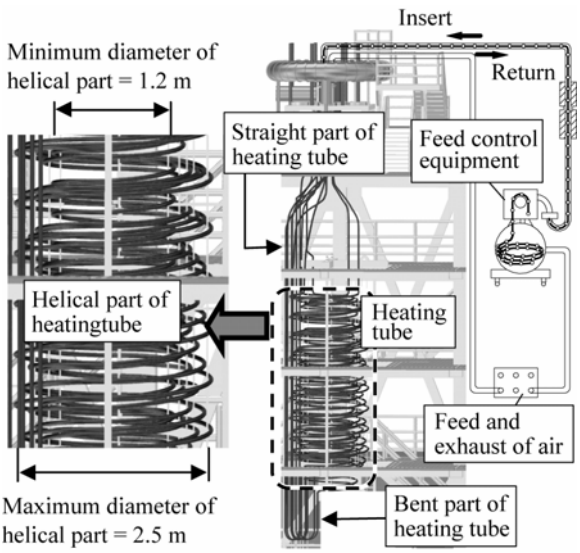

Fig. 1. Mock-up test facility.

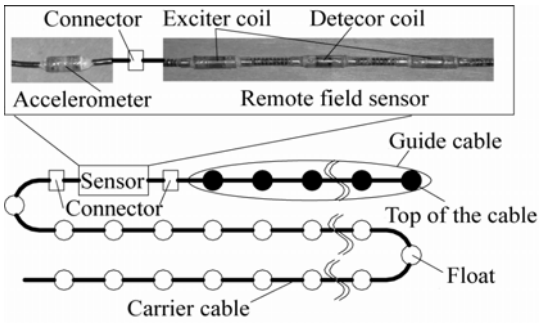

Fig. 2. ECT probe and accelerometer.

air flow of the return process. The probe passes through the heating tube very quickly unless the feed control equipment, which is shown in Fig. 1, regulates the feeding speed. An axial force of which direction is opposite to the moving direction acts on the probe from the feed control equipment. Thus, a tensile force acts on the probe in the insertion process on the average, while a compressive force acts on the probe in the return process. The detection of defects can be operated both in the insertion and the return processes, and inspections in both processes are desirable in order to ensure the reliability of the inspection.

2.1 Summary of the experimental results

Experimental results by using the mock-up (Inoue et al., 2007) are summarized as follows.

a. During the inspection, the RF sensor transmits two signals X and Y, which are output voltage from the detector coil. Their directions are perpendicular to each other, and also perpendicular to the axial direction of the helical tube as shown in Fig. 3(a). Usually, the directions of X and Y do not correspond to the normal and the binormal ones of the helical tube. Fig. 3(b) shows RF signal at the carrier velocity of 200 mm/s when the sensor part passes through the sensitivity test piece. Signals X and Y generate fluctuations in opposite directions at the same time, but the amplitudes are different from each other. In Fig. 3(c), the Lissajous' figures for signals X and Y are illustrated.

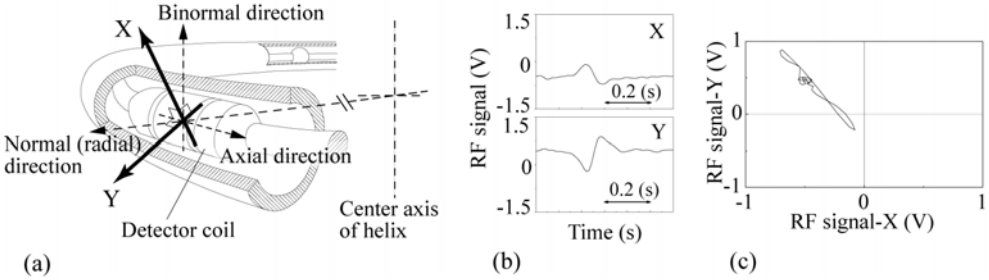

Fig. 3. (a) Two RF signals X and Y, (b) RF signals at the test piece and (c) its Lissajous' figure.

b. The total length of the heating tube is about 90 m. The length of the helical part is about 60m (see Fig. 1). RF signals of X, Y and accelerations nearby the sensor in the insertion process are shown in Fig. 4(a and b), respectively. The sensor passed the helical part of the heating tube in the shaded area of Fig. 4(a and b) and an approximate length of the

probe inserted into the helical part is also indicated. Large impulsive signals at positions A and B shown in Fig. 4(a) were caused by metallic flanges to connect the both ends of the acrylic fluoroscopy tube. The acrylic fluoroscopy tube can be set up at either position A or B in order to observe the movement of probe by high-speed camera. Although the impulsive signals are large noises on the RF signals, we ignore them because the actual heating tubes are not equipped with the acrylic fluoroscopy tube and metallic flanges. On one hand, the small impulsive signals in the RF signals like short beards in the region of the helical tube occurring at equal intervals. These signals are generated as the sensor part passes through the metallic outer support of the heating tube. The small impulsive signal is called "support signal". Although the support signal is a kind of noise on the RF signals, the discrimination between the attenuation and the support signal is not discussed in this study, because the actual metallic outer supports are different from the ones of the mock-up. We focus on the relationship between the vibration and the RF signal noise.

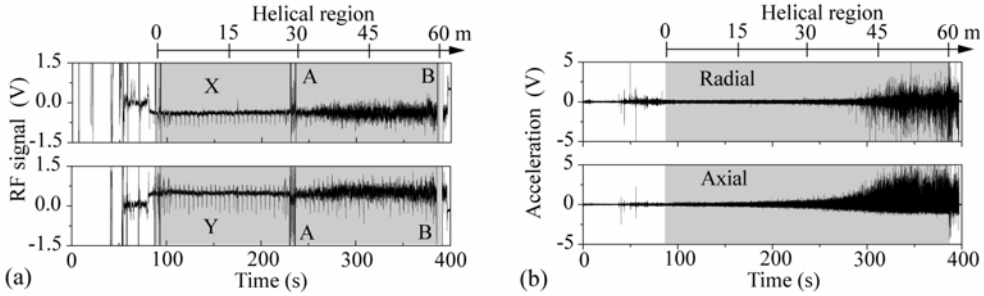

Fig. 4. (a and b) RF signal and acceleration in insertion process.

c. The accelerations shown in Fig. 4(b) were measured by an accelerometer, which was specially arranged for the experiment, located nearby the sensor as shown in Fig. 2. The directions of the acceleration were lateral and longitudinal of the probe and correspond to the radial and axial directions of the helical heating tube. From Fig. 4(b), the vibration of the probe rapidly increased after the sensor passed through the middle position of the helical part. At the same time, the noises were raised in the RF signals and kept a large value until the insertion process finished. It means that there was adequate correlation between the probe vibration and RF signal noise. In addition, we confirmed that a noticeable peak in the frequency analysis (about 20 Hz) appeared in both the axial and the radial vibrations of the probe. Both vibrations were weakly coupled and the probe showed an inchworm-like motion.
d. In the case of non-feeding, no vibration of the probe occurred even if the dry compressed air streamed into the heating tube. No RF signal noise was also appeared. It was expected that the vibration of the probe was mainly caused by a frictional force between the floats and the inner wall of the heating tube, and the fluid force was not an essential factor of the vibration.
e. The vibration of the probe in the return process was smaller than the one in the insertion process. There was no noticeable peak in the frequency analysis of the vibration in the return process.
f. The vibration of the probe became small in the case of low feeding speed, large helical diameter and low supply rate of the air flow.

g. It was found that the RF signal noise highly correlated with radial vibration of the probe. A long guide cable made the RF signal noise small because it was effective in suppressing the radial vibration. In addition, a large size of float attached to the guide cable was also effective in suppressing the vibration.

In this study, only the vibration of the probe is focused on because there was a certain correlation between the probe vibration and RF signal noise. The inspection of the attenuation of the wall thickness is operated in both the insertion and the return processes in order to perform a firm inspection. In this study, the vibration of the insertion process is focused on since it is larger than the one of the return process as mentioned above e.

2.2 Analytical model of probe

The analytical model is obtained under the following simplifications so that the numerical analysis can be implemented as easily as possible.

a. The heating tubes consist of straight, helical and bending parts as shown in Fig. 1. The vibration of the probe always occurred in the helical part, and it did not occur in the other parts of the heating tubes. Therefore, only the helical part of the heating tube is considered.
b. The length of the actual probe becomes longer as the insertion process goes on. However, it is difficult to treat a probe with time varying length. On one hand, if a vibrating probe, which is sufficiently inserted in the helical tube, stops feeding and restarts, the vibration of the probe is always reproduced. It follows that a probe with a constant length can be regarded as a momentary situation in which the actual time varying length of probe just reached the length. Hence, many probes with constant length (each length is different from one another) can be substitutes for the actual probe with time varying length. In this paper, the length of the probe is assumed to be constant and many probes with constant length are treated in order to cope with the actual probe with time varying length.
c. Contact points between the floats and the inner wall of the heating tube are always generated at the inside of the helical tube as shown in Fig. 5, because tensile force acts on the probe in the insertion process.

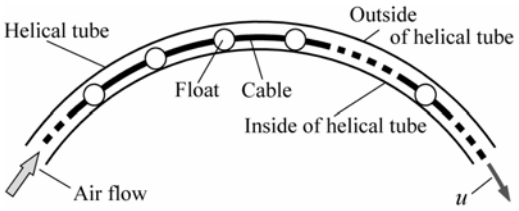

Fig. 5. Analytical model of probe in helical tube.

d. The vertical motion of the probe is disregarded. The motion of the probe is restricted within the horizontal plane. Thus, the probe moves in a circular tube placed in the horizontal plane as shown in Fig. 6.
e. The movement of the probe is modeled as illustrated in Fig. 5. The probe moves in the heating tube at a constant speed u from the left-hand side to the right-hand side of Fig. 5. The dry compressed air also flows inside the tube in the same direction of the movement of probe. Secondary flow around the floats and cable is neglected.

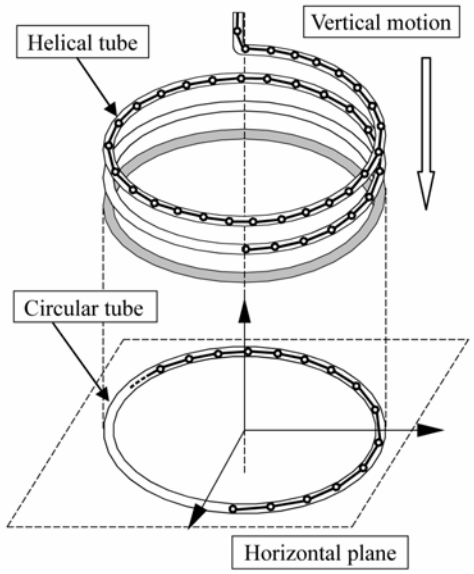

Fig. 6. Actual and analytical heating tube.

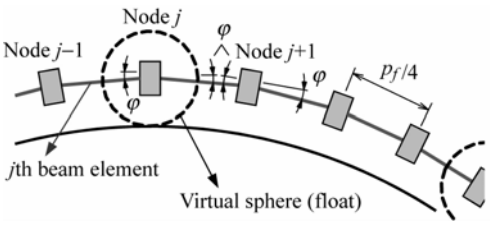

Fig. 7. Lumped mass modeling.

Based on the simplifications, the probe is modeled as a lumped mass system as shown in Fig. 7. The cable is equally divided, and rigid bodies which possess mass and moment of inertia, are put to each divided point. Each section spaced by floats is divided into four by taking a balance between the float pitch p_f and diameter of the cable d_c into consideration. The analytical model is formed by a connection of the rigid bodies and massless beams in series as shown in Fig. 7. The probe can be regarded as almost uniform because it was made by a continuous cable and lightweight spherical floats which are attached to the cable. Thus, the mass and moment of inertia of each rigid body are assumed to be identical and given as follows:

$$m = \rho_c \frac{p_f}{4}, \quad J = m\left[\frac{1}{12}\left(\frac{p_f}{4}\right)^2 + \frac{d_c^2}{16}\right] \tag{1}$$

where ρ_c is mass per unit length of probe, including the mass of the cable and floats. The moment of inertia J was obtained as a rigid column with diameter d_c and height $p_f/4$. Virtual spheres are assumed to be around the rigid bodies which occupy the place where the floats

originally existed. The diameter of the virtual spheres is equal to one of the floats and is common to all spheres. The spheres fill the role of the floats, which are subjected to the drag force of air flow and are in contact with the inner wall of the heating tube. Contact forces and frictional forces from the inner wall of the heating tube also act on the virtual sphere. The forces are transmitted to the rigid bodies through the virtual sphere. The mass and the moment of inertia of the RF sensor are also assumed to be m and J without a special treatment.

Each rigid body is called "Node" and the left- and the righ-thand ends of the system are defined as node 0 and node n, respectively. The beam element between the node j and $j-1$ is called jth beam element. Each of the beam elements is assumed to be straight and slantingly connects with rigid bodies at both ends as shown in Fig. 7. The slant connection is due to the curvature of the helical heating tube and the slanting angle φ is given as:

$$\varphi = \sin^{-1}[p_f / (4d_h)] \tag{2}$$

where d_h is a diameter of the helix.

2.3 Equation of motion

In this paper, variables with head symbol and subscripts have following principles:

a. Variables with subscript j represent the physical quantities related to node j or the jth beam element.
b. Variables with and without head symbol "–" represent the physical quantities on the left- and the right-hand side of node, respectively.

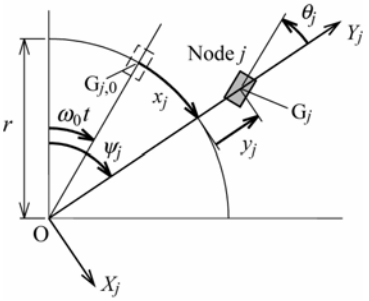

Fig. 8. Polar coordinate.

Since the probe goes into the helical (circular, under the assumption d of Section 2.2) tube at a constant speed, the motion of the rigid body at node j is represented in a polar coordinate O–X_jY_j as shown in Fig. 8. The point O in Fig. 8 corresponds to the center of the helix (or circle) and the X_j-axis points toward a center of gravity of the rigid body G_j. Supposing that a center of gravity of the rigid body without stretch and lateral motion of the probe is denoted $G_{j,0}$, the point of $G_{j,0}$ turns around the center O at a constant angular velocity ω_0 which is given as:

$$\omega_0 = u / r, \quad r = d_h / 2 \tag{3}$$

where r is the radius of the helix. The relative movement of the rigid body at node j with respect to the unstretched probe is represented as an axial displacement $x_j(t)$ (arc coordinate

along the helix) from $G_{j,0}$, a radial displacement $y_j(t)$ from $G_{j,0}$ and a rotation $\theta_j(t)$ around G_j as shown in Fig. 8. Physical quantities such as $x_j(t)$, $y_j(t)$, $\theta_j(t)$, etc., are functions of time t in principle but the argument (t) is omitted in Fig. 8. The root of the probe, node 0, is assumed to move at the regulation speed u without lateral motion and rotation around $G_0 = G_{0,0}$. So, physical quantities on node 0 are fixed as: $x_0(t) = y_0(t) = \theta_0(t) = 0$.

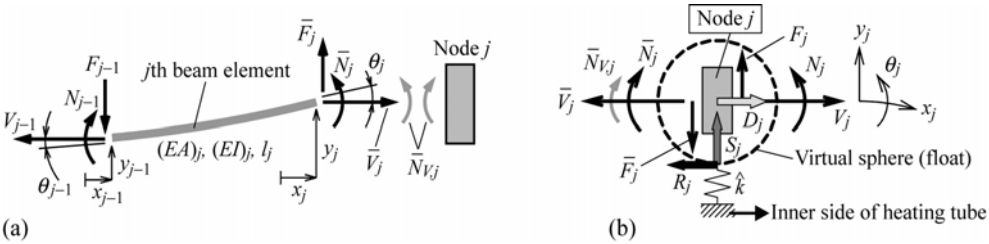

Fig. 9. State variables and external forces at (a) both ends of the jth beam element and (b) node j.

State variables at both ends of the jth beam element and the positive direction of the variables are shown in Fig. 9(a), where $\bar{V}_j(t)$, $V_{j-1}(t)$ are axial forces, $\bar{F}_j(t)$, $F_{j-1}(t)$ are shearing forces and $\bar{N}_j(t)$, $N_{j-1}(t)$ are moment of forces. Displacement vectors and force vectors are defined as follows:

$$\begin{aligned} \boldsymbol{d}_{j-1}(t) &= \{x(t), y(t), \theta(t)\}_{j-1}^{\mathrm{T}}, \quad \boldsymbol{d}_j(t) = \{x(t), y(t), \theta(t)\}_j^{\mathrm{T}} \\ \boldsymbol{f}_{j-1}(t) &= \{V(t), F(t), N(t)\}_{j-1}^{\mathrm{T}}, \quad \bar{\boldsymbol{f}}_j(t) = \{\bar{V}(t), \bar{F}(t), \bar{N}(t)\}_j^{\mathrm{T}} \end{aligned} \tag{4}$$

where superscript "T" denotes transpose. Argument (t) is omitted in Fig. 9 as same as in Fig. 8. The displacements $x_j(t)$, $y_j(t)$ and $x_{j-1}(t)$, $y_{j-1}(t)$ should be represented in a polar coordinate as shown in Fig. 8 because the jth beam element connects with the rigid bodies of node j and $j-1$. However, inertia forces of polar coordinate do not act on the jth beam element because the beam elements are assumed to be massless. In addition, the curvature of $x_j(t)$ and $x_{j-1}(t)$ are negligible since $x_j(t)$ and $x_{j-1}(t)$ are sufficiently smaller than the diameter of the helix d_h. Hence, the displacements are approximately treated in a local orthogonal coordinate, and the relationships of the state variables are represented in following simple forms.

$$\boldsymbol{d}_j(t) = \boldsymbol{L}_j^{\mathrm{T}} \boldsymbol{d}_{j-1}(t) + \boldsymbol{F}_j \bar{\boldsymbol{f}}_j(t) \tag{5}$$

$$\boldsymbol{f}_{j-1}(t) = \boldsymbol{L}_j \bar{\boldsymbol{f}}_j(t) \tag{6}$$

where

$$\boldsymbol{L}_j = \begin{bmatrix} 1 & 0 & 0 \\ 0 & 1 & 0 \\ 0 & l_j & 1 \end{bmatrix}, \quad \boldsymbol{F}_j = \begin{bmatrix} a_x & 0 & 0 \\ 0 & a_y & \gamma \\ 0 & \gamma & \beta \end{bmatrix}_j, \quad (a_x, a_y, \beta, \gamma)_j = \left(\frac{l}{EA}, \frac{l^3}{3EI}, \frac{l}{EI}, \frac{l^2}{2EI} \right)_j$$

where l_j, $(EA)_j$ and $(EI)_j$ are length, tensile rigidity and flexural rigidity of the jth beam element. Eqs. (5) and (6) are arranged as follows:

$$\begin{bmatrix} \boldsymbol{f}_{j-1}(t) \\ \overline{\boldsymbol{f}}_j(t) \end{bmatrix} = \begin{bmatrix} -\boldsymbol{L}_j\boldsymbol{F}_j^{-1}\boldsymbol{L}_j^{\mathrm{T}} & \boldsymbol{L}_j\boldsymbol{F}_j^{-1} \\ -\boldsymbol{F}_j^{-1}\boldsymbol{L}_j^{\mathrm{T}} & \boldsymbol{F}_j^{-1} \end{bmatrix} \begin{bmatrix} \boldsymbol{d}_{j-1}(t) \\ \boldsymbol{d}_j(t) \end{bmatrix} \tag{7a}$$

The coefficient matrix of the right-hand side of Eq. (7a) represents a stiffness matrix of *j*th beam element, and it also represents the rigidity of the cable. In addition, since the cable shows a considerable damping property, we introduce a damping term associated with the velocity vectors $\dot{\boldsymbol{d}}_j(t)$ and $\dot{\boldsymbol{d}}_{j-1}(t)$. In this study, a proportional viscous damping (proportional coefficient δ) is adopted. Thus, the relationship of the state variables at both ends of the *j*th beam element is represented as follows:

$$\begin{bmatrix} \boldsymbol{f}_{j-1}(t) \\ \overline{\boldsymbol{f}}_j(t) \end{bmatrix} = \begin{bmatrix} -\boldsymbol{L}_j\boldsymbol{F}_j^{-1}\boldsymbol{L}_j^{\mathrm{T}} & \boldsymbol{L}_j\boldsymbol{F}_j^{-1} \\ -\boldsymbol{F}_j^{-1}\boldsymbol{L}_j^{\mathrm{T}} & \boldsymbol{F}_j^{-1} \end{bmatrix} \begin{bmatrix} \boldsymbol{d}_{j-1}(t) \\ \boldsymbol{d}_j(t) \end{bmatrix} + \delta \begin{bmatrix} -\boldsymbol{L}_j\boldsymbol{F}_j^{-1}\boldsymbol{L}_j^{\mathrm{T}} & \boldsymbol{L}_j\boldsymbol{F}_j^{-1} \\ -\boldsymbol{F}_j^{-1}\boldsymbol{L}_j^{\mathrm{T}} & \boldsymbol{F}_j^{-1} \end{bmatrix} \begin{bmatrix} \dot{\boldsymbol{d}}_{j-1}(t) \\ \dot{\boldsymbol{d}}_j(t) \end{bmatrix} \tag{7b}$$

The second term of the right-hand side of Eq. (7b) corresponds to a proportional viscous damping.

A following couple (moment of force) due to the axial force is generated.

$$N_{V,j}(t) = \overline{V}_j(t)[y_j(t) - y_{j-1}(t)] = V_{j-1}(t)[y_j(t) - y_{j-1}(t)] \tag{8}$$

However, this couple is not considered in Eq. (7b). Since the axial force generated in the cable is very large, the effect of this moment of force is not negligible. It is substituted by a moment of force $\overline{N}_{V,j}(t)$ which equilibrates $N_{V,j}(t)$ and acts on the *j*th beam element from node *j* as shown in Fig. 9(a). A reaction of $\overline{N}_{V,j}(t)$ also acts on the node *j*. Assuming that the elastic deformation of the beam element is small, the following approximation is available:

$$\overline{N}_{V,j}(t) = \overline{V}_j(t)[y_j(t) - y_{j-1}(t)] \cong \overline{V}_j(t) l_j \theta_j(t) \tag{9}$$

State variables at node *j* are shown in Fig. 9(b), where the node is regarded as a float so that a virtual sphere and forces acting on the sphere are also depicted in Fig. 9(b). Since node j possesses mass and moment of inertia, inertia forces of polar coordinate, such as a centrifugal force and Coriolis force, act on node j. Hence, displacements $x_j(t)$, $y_j(t)$ and rotational angle $\theta_j(t)$ are treated in the polar coordinate as shown in Fig. 8.

Drag force $D_j(\dot{x}_j)$ acting on the float by air flow, which is the driving force of the probe, is represented as follows:

$$D_j(\dot{x}_j) = (1/2) c_D \rho_f (A_f - A_c) v_{rel}(\dot{x}_j) |v_{rel}(\dot{x}_j)| \tag{10}$$

where $v_{rel}(\dot{x}_j) = Q/(a - A_c) - u - \dot{x}_j(t)$, c_D = 0.44 is the coefficient of drag force, ρ_f is the air flow density, $A_f = \pi d_f^2/4$ is the cross-section of float, d_f is the diameter of float, $A_c = \pi d_c^2/4$ is the cross-section of cable, Q is the supply rate of air flow, $a = \pi d_{in}^2/4$ is the cross-section of heating tube and d_{in} is the inner diameter of heating tube.

The loss of the pressure head is not considered here.

A contact spring, of which spring constant is $\hat{k}$, is assumed to exist between the floats and the inner wall of the heating tube as shown in Fig. 9(b). The float contacts with the inner wall through the contact spring when the radial displacement $y_j(t) < 0$, and a reaction force $S_j(y_j)$ acts on the float from the inner wall of the heating tube. Positive direction of $S_j(y_j)$ is defined as shown in Fig. 9(b) and hence $S_j(y_j)$ is represented as:

$$S_j(y_j) = -k_j(y_j)\, y_j(t), \quad k_j(y_j) = \begin{cases} 0 & : y_j(t) \geq 0 \\ \hat{k} & : y_j(t) < 0 \end{cases} \tag{11}$$

where the spring constant $\hat{k}$ is assumed to be common to all floats. The Coulomb friction $R_j(y_j, \dot{x}_j, \theta_j)$, which is proportional to $S_j(y_j)$, also acts on the float. Since the direction of Coulomb friction is determined by the relative velocity at the contact point between the float and the inner wall, Coulomb friction is represented as follows:

$$\begin{aligned} R_j(y_j, \dot{x}_j, \dot{\theta}_j) &= \mu_j(\dot{x}_j, \dot{\theta}_j) S_j(y_j) = -\mu_j(\dot{x}_j, \dot{\theta}_j) k_j(y_j)\, y_j(t) \\ \mu_j(\dot{x}_j, \dot{\theta}_j) &= \begin{cases} \mu_d & : u + \dot{x}_j(t) + \dot{\theta}_j(t)\, d_f / 2 \geq 0 \\ -\mu_d & : u + \dot{x}_j(t) + \dot{\theta}_j(t)\, d_f / 2 < 0 \end{cases} \end{aligned} \tag{12}$$

where the coefficient of kinetic friction μ_d is also assumed to be common to all floats.
In addition, node j is subjected to axial forces $\bar{V}_j(t), V_j(t)$, shearing forces $\bar{F}_j(t), F_j(t)$ and moment of forces $\bar{N}_j(t), N_j(t)$ from the beam elements connecting to the node j as shown in Fig. 9(b). Furthermore, the moment of force $\bar{N}_{V,j}(t)$ due to the axial force, which is treated as a time varying rotational spring [see Eq. (9)], also acts on the node j. Since the movement of the rigid body is represented in a polar coordinate (Fig. 8), accelerations of the rigid body at node j are represented as:

$$X_j\text{-direction}: \; r_j'\ddot{\psi}_j + 2\dot{r}_j'\dot{\psi}_j, \;\; Y_j\text{-direction}: \; \ddot{r}_j' - r_j'\dot{\psi}_j^2, \;\; \text{rotation}: \; \ddot{\theta}_j - \ddot{\psi}_j \tag{13}$$

where $r_j' = r + y_j(t)$, $\psi_j = \omega_0 t + x_j(t)/r$, $\dot{\psi}_j = \omega_j(\dot{x}_j) = \omega_0 + \dot{x}_j(t)/r$, $\ddot{\psi}_j = \dot{\omega}_j(\dot{x}_j) = \ddot{x}_j(t)/r$.
Thus, the equation of motion of the rigid body at node j is expressed as follows with respect to X_j-, Y_j-directions and rotation.

$$\begin{aligned} & mr\left(1 + \frac{y_j(t)}{r}\right)\frac{\ddot{x}_j(t)}{r} + 2m\omega_j(\dot{x}_j)\dot{y}_j(t) = -R_j(y_j, \dot{x}_j, \dot{\theta}_j) + V_j(t) - \bar{V}_j(t) \\ & m\ddot{y}_j(t) - mr\left(1 + \frac{y_j(t)}{r}\right)\omega_j^2(\dot{x}_j) = S_j(y_j) + F_j(t) - \bar{F}_j(t) \\ & J_j\left(\ddot{\theta}_j - \frac{\ddot{x}_j(t)}{r}\right) = -R_j(y_j, \dot{x}_j, \dot{\theta}_j)\frac{d_f}{2} - \bar{N}_{V,j}(t) \end{aligned} \tag{14}$$

Eq. (14) is arranged as follows with an approximation: $1 + y_j(t)/r \cong 1$.

$$\boldsymbol{M}\ddot{\boldsymbol{d}}_j(t) + \boldsymbol{C}_j(\dot{x}_j)\dot{\boldsymbol{d}}_j(t) + \boldsymbol{K}_j(y_j, \dot{x}_j, \dot{\theta}_j, \bar{V}_j)\boldsymbol{d}_j(t) = \tilde{\boldsymbol{q}}_j(\dot{x}_j) + \boldsymbol{f}_j(t) - \bar{\boldsymbol{f}}_j(t) \tag{15}$$

where

$$\boldsymbol{M} = \begin{bmatrix} m & 0 & 0 \\ 0 & m & 0 \\ -J/r & 0 & J \end{bmatrix}, \quad \boldsymbol{C}_j(\dot{x}_j) = \begin{bmatrix} 0 & 2m\omega_j(\dot{x}_j) & 0 \\ 0 & 0 & 0 \\ 0 & 0 & 0 \end{bmatrix}$$

$$\boldsymbol{K}_j(y_j, \dot{x}_j, \dot{\theta}_j, \bar{V}_j) = \begin{bmatrix} 0 & -\mu_j(\dot{x}_j, \dot{\theta}_j) k_j(y_j) & 0 \\ 0 & k_j(y_j) & 0 \\ 0 & -\mu_j(\dot{x}_j, \dot{\theta}_j) k_j(y_j)\, d_f/2 & \bar{V}_j(t) l_j \end{bmatrix}, \quad \tilde{\boldsymbol{q}}_j(\dot{x}_j) = \{D_j(\dot{x}_j), mr\omega_j^2(\dot{x}_j), 0\}^{\mathrm{T}}$$

The matrix $\boldsymbol{C}_j(\dot{x}_j)$ does not represent a damping matrix here, but a kind of Coriolis force as a term of $\boldsymbol{C}_j(\dot{x}_j)\dot{\boldsymbol{d}}_j(t)$. As for a damping, a proportional viscous damping, the second term of the right-hand side of Eq. (7b), is considered. An element $mr\omega_j^2(\dot{x}_j)$ of the vector $\tilde{\boldsymbol{q}}_j(\dot{x}_j)$ represents a centrifugal force in a polar coordinate.
If the rigid body of node j does not correspond to a float, it does not contact with the inner wall of the heating tube and is free from the drag force $D_j(\dot{x}_j)$. The equation of motion of such a rigid body is similarly represented as Eq. (15) by setting $D_j(\dot{x}_j)$, $\hat{k}$ and μ_d to be zero.

3. Step-by-step time integration scheme by utilizing the Transfer Influence Coefficient Method

3.1 Step-by-step time integration scheme

Time historical response of the probe can be computed by applying a step-by-step time integration scheme to the equation of motion obtained in Section 2. Displacement $\boldsymbol{d}_j(t)$, velocity $\dot{\boldsymbol{d}}_j(t)$ and acceleration $\ddot{\boldsymbol{d}}_j(t)$ vectors are successively computed at an interval of time step size Δt. For a large scale structure, the Newmark-β method and the Wilson-θ method (Belytschko and Hughes, 1983) are usually employed as the step-by-step time integration scheme. Velocity and acceleration vectors at time $t_i = i\Delta t$ are usually expressed as a linear function of displacement vector in an implicit method such as the Newmark-β and the Wilson-θ methods. The formulation is given as follows:

$$\ddot{\boldsymbol{d}}_j(t_i) = B_a \boldsymbol{d}_j(t_i) + \boldsymbol{h}_{a,j}(t_{i-1}), \quad \dot{\boldsymbol{d}}_j(t_i) = B_v \boldsymbol{d}_j(t_i) + \boldsymbol{h}_{v,j}(t_{i-1}) \tag{16}$$

where the coefficients B_a, B_v are the constants decided in each step-by-step integration scheme and $\boldsymbol{h}_{a,j}(t_i-1)$, $\boldsymbol{h}_{v,j}(t_i-1)$ are functions of displacement, velocity and acceleration vectors before the time t_{i-1} (see Table 1). The coefficients for the Newmark-β and the Wilson-θ methods are listed in Table 1.
Substituting Eq. (16) into Eq. (15), the equation of motion is transformed into following formula:

$$\boldsymbol{P}_j(t_{i-1})\,\boldsymbol{d}_j(t_i) = \boldsymbol{q}_j(t_{i-1}) + \boldsymbol{f}_j(t_i) - \bar{\boldsymbol{f}}_j(t_i) \tag{17}$$

where

$$\boldsymbol{P}_j(t_{i-1}) = B_a \boldsymbol{M} + B_v \boldsymbol{C}_j(t_{i-1}) + \boldsymbol{K}_j(t_{i-1}), \quad \boldsymbol{q}_j(t_{i-1}) = \tilde{\boldsymbol{q}}_j(t_{i-1}) - \boldsymbol{M}\,\boldsymbol{h}_{a,j}(t_{i-1}) - \boldsymbol{C}_j(t_{i-1})\,\boldsymbol{h}_{v,j}(t_{i-1})$$

The state variables $y_j(t_i)$, $\dot{x}_j(t_i)$, $\dot{\theta}_j(t_i)$ and $\bar{V}_j(t_i)$ in the $\boldsymbol{C}_j(\dot{x}_j)$, $\boldsymbol{K}_j(y_j,\dot{x}_j,\dot{\theta}_j,\bar{V}_j)$ and $\tilde{\boldsymbol{q}}_j(\dot{x}_j)$ of

	B_a	$\mathbf{h}_{a,j}(t_{i-1})$	B_v	$\mathbf{h}_{v,j}(t_{i-1})$
Newmark-β	$\frac{1}{\beta\Delta t^2}$	$\frac{-1}{\beta\Delta t^2}\left[\mathbf{d}_j(t_{i-1})+\Delta t\,\dot{\mathbf{d}}_j(t_{i-1})+\left(\frac{1}{2}-\beta\right)\Delta t^2\ddot{\mathbf{d}}_j(t_{i-1})\right]$	$\frac{\gamma}{\beta\Delta t}$	$\dot{\mathbf{d}}_j(t_{i-1})+\Delta t[(1-\gamma)\ddot{\mathbf{d}}_j(t_{i-1})+\gamma\,\mathbf{h}_{a,j}(t_{i-1})]$
Wilson-θ	$\frac{6}{(\theta\Delta t)^2}$	$\frac{-6}{(\theta\Delta t)^2}\left[\mathbf{d}_j(t_{i-1})+\theta\Delta t\,\dot{\mathbf{d}}_j(t_{i-1})+\frac{(\theta\Delta t)^2}{3}\ddot{\mathbf{d}}_j(t_{i-1})\right]$	$\frac{3}{\theta\Delta t}$	$\frac{-3}{\theta\Delta t}\left[\mathbf{d}_j(t_{i-1})+\frac{2\theta\Delta t}{3}\dot{\mathbf{d}}_j(t_{i-1})+\frac{(\theta\Delta t)^2}{6}\ddot{\mathbf{d}}_j(t_{i-1})\right]$

Table 1. Coefficients for step-by-step solution scheme.

Eq. (15) are replaced by the ones of one time step before $y_j(t_{i-1})$, $\dot{x}_j(t_{i-1})$, $\dot{\theta}_j(t_{i-1})$ and $\bar{V}_j(t_{i-1})$, respectively. Thus, the coefficients $\boldsymbol{C}_j(\dot{x}_j)$, $\boldsymbol{K}_j(y_j,\dot{x}_j,\dot{\theta}_j,\bar{V}_j)$ and vector $\tilde{\boldsymbol{q}}_j(\dot{x}_j)$ are known at the time t_i. These are expressed as $\boldsymbol{C}_j(t_{i-1})$, $\boldsymbol{K}_j(t_{i-1})$ and $\tilde{\boldsymbol{q}}_j(t_{i-1})$ in Eq. (17). It implies that time delay components are generated in Eq. (17).
Substituting Eq. (16) into Eq. (7b), we have transformed relationships of state variables between both ends of a beam element.

$$\boldsymbol{d}_j(t_i)=\boldsymbol{L}_j^{\mathrm{T}}\boldsymbol{d}_{j-1}(t_i)+\frac{1}{1+\delta B_v}\boldsymbol{F}_j\bar{\boldsymbol{f}}_j(t_i)+\frac{\delta}{1+\delta B_v}[\boldsymbol{L}_j^{\mathrm{T}}\boldsymbol{h}_{v,j-1}(t_{i-1})-\boldsymbol{h}_{v,j}(t_{i-1})] \tag{18}$$

Solving Eqs. (17), (18) and (6) simultaneously with respect to all nodes (j : 0 – n) yields displacement vectors $\boldsymbol{d}_j(t_i)$ of all nodes. Velocity and acceleration vectors $\dot{\boldsymbol{d}}_j(t_i)$ and $\ddot{\boldsymbol{d}}_j(t_i)$ are given by Eq. (16) according to the obtained displacement vector $\boldsymbol{d}_j(t_i)$. The obtained $\boldsymbol{d}_j(t_i)$, $\dot{\boldsymbol{d}}_j(t_i)$ and $\ddot{\boldsymbol{d}}_j(t_i)$ yield $\boldsymbol{h}_{a,j}(t_i)$, $\boldsymbol{h}_{v,j}(t_i)$, (see Table 1), then displacement, velocity and acceleration vectors at the next time step $\boldsymbol{d}_j(t_{i+1})$, $\dot{\boldsymbol{d}}_j(t_{i+1})$ and $\ddot{\boldsymbol{d}}_j(t_{i+1})$ are similarly obtained. Step-by-step time integration scheme proceeds in the same way.
However, numerical instability possibly happens in the step-by-step time integration because the reaction force $S_j(y_j)$ and the frictional force $R_j(y_j,\dot{x}_j,\dot{\theta}_j)$ involve the time delay components in addition to the strong non-linearity in Eq. (17). Although the Newmark-β method ($\beta = 1/4$, $\gamma = 1/2$) and theWilson-θ method ($\theta = 1.4$) are absolutely stable to linear systems, numerical instability often happens in the both methods in the treatment of non-linear systems (Crisfield and Shi, 1996; Xie, 1996). A way to avoid the numerical instability is to use a small time step size but it takes a great deal of computational costs. Furthermore, Eqs. (17), (18) and (6) are solved as simultaneous equations of which the degree of freedom corresponds to that of the whole system. The total computational costs will be extremely large.
The TICM, which was developed by one of the authors, is a useful method to solve Eqs. (17), (18) and (6). The TICM does not solve Eqs. (17), (18) and (6) simultaneously, but solves them through a recursive algorithm. It makes the computation very fast. The concept of the TICM is based on a transmission of physical quantities from one end of structure to the other end of structure. This concept is similar to the Transfer Matrix Method (Pestel and Leckie, 1963, hereafter: TMM). However, the TICM has an advantage in computational speed since the dimensions of matrices and vectors used in the algorithm are smaller than the ones of the TMM. In addition, the TICM also has an advantage in computational accuracy. The TICM is free from a numerical instability, which sometimes happens in the TMM under a certain condition, for example, treatment of rigid supports, computation of high frequency range, etc. The TICM is good at a longitudinally extended structure, which includes the probe discussed here, according to its concept. Therefore, we employ the TICM as a device to compute the displacement vectors $\boldsymbol{d}_j(t_i)$. Even a standard computer can perform efficient computation by utilizing the TICM.

3.2 The Transfer Influence Coefficient Method

The concept of the TICM is illustrated in Fig. 10. The structure enclosed with a broken line in Fig. 10(a) schematically shows a connection of rigid bodies, from node 0 to node $j-1$, by means of beam elements. A curvature of the probe, spheres (floats) and contact springs are omitted in Fig. 10. Connections of jth beam element and node j follow as shown in Fig. 10(a). The repetition of the connection brings to the completion of the whole structure (probe).

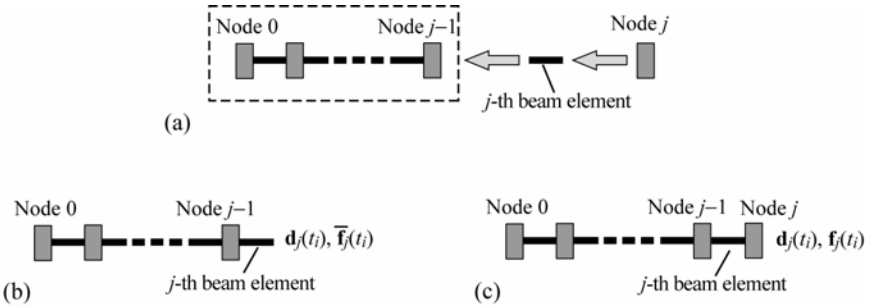

Fig. 10. Concept of the TICM: (a) connections of jth beam element and node j. (b) After the connection of jth beam element, and (c) after the following connection of node j.

This is the concept of the TICM. A structure after the connection of jth beam element, and following connection of node j are illustrated in Fig. 10(b and c), respectively. In the formulation of the TICM for a step-by-step time integration, a relationship between the displacement vector $\boldsymbol{d}_j(t_i)$ and the force vector $\overline{\boldsymbol{f}}_j(t_i)$ illustrated in Fig. 10(b), before the connection of node j, is defined as follows:

$$\boldsymbol{d}_j(t_i) = \overline{\boldsymbol{T}}_j(t_i)\,\overline{\boldsymbol{f}}_j(t_i) + \overline{\boldsymbol{s}}_j(t_i) \tag{19}$$

We call the 3×3 square matrix $\overline{\boldsymbol{T}}_j(t_i)$ and three-dimensional vector $\overline{\boldsymbol{s}}_j(t_i)$ a dynamic influence coefficient matrix and an additional vector of the left-hand side of node j, respectively. The additional vector $\overline{\boldsymbol{s}}_j(t_i)$ represents an influence of external forces, which act on the preceding nodes 0 to $j-1$, to displacement vector at node j.
Similarly, a relationship between $\boldsymbol{d}_j(t_i)$ and $\boldsymbol{f}_j(t_i)$ illustrated in Fig. 10(c), after the connection of node j, is defined as:

$$\boldsymbol{d}_j(t_i) = \boldsymbol{T}_j(t_i)\,\boldsymbol{f}_j(t_i) + \boldsymbol{s}_j(t_i) \tag{20}$$

where the matrix $\boldsymbol{T}_j(t_i)$ and the vector $\boldsymbol{s}_j(t_i)$ are called a dynamic influence coefficient matrix and an additional vector of the right-hand side of node j, respectively. The additional vector $\boldsymbol{s}_j(t_i)$ represents an influence of external forces, which act on the preceding nodes 0 to $j-1$ and newly connected node j.
In the algorithm of the TICM, the matrices $\overline{\boldsymbol{T}}_j(t_i)$, $\boldsymbol{T}_j(t_i)$ and vectors $\overline{\boldsymbol{s}}_j(t_i)$, $\boldsymbol{s}_j(t_i)$ are successively computed from node 0 (root of the probe) to node n (top of the probe) at first. Subsequently, the displacement vectors are computed in the reverse order from node n to node 0. Substituting Eq. (20) with subscript $j-1$ and Eq. (6) into Eq. (18) yields

$$\begin{aligned}\boldsymbol{d}_j(t_i) = &\left[\boldsymbol{L}_j^{\mathrm{T}}\boldsymbol{T}_{j-1}(t_i)\boldsymbol{L}_j\,\overline{\boldsymbol{f}}_j(t_i) + \frac{1}{1+\delta B_v}\boldsymbol{F}_j\right]\overline{\boldsymbol{f}}_j(t_i) \\ &+ \boldsymbol{L}_{j-1}^{\mathrm{T}}\boldsymbol{s}_j(t_i) + \frac{\delta}{1+\delta B_v}[\boldsymbol{L}_j^{\mathrm{T}}\boldsymbol{h}_{v,j-1}(t_{i-1}) - \boldsymbol{h}_{v,j}(t_{i-1})]\end{aligned} \tag{21}$$

Comparing Eq. (21) with Eq. (19), we have

$$\overline{\boldsymbol{T}}_j(t_i) = {}^{t}\boldsymbol{L}_j\boldsymbol{T}_{j-1}(t_i)\boldsymbol{L}_j + \frac{1}{1+\delta B_v}\boldsymbol{F}_j \tag{22a}$$

$$\bar{\boldsymbol{s}}_j(t_i) = {}^t\boldsymbol{L}_j\,\boldsymbol{s}_{j-1}(t_i) + \frac{\delta}{1+\delta B_v}[\,{}^t\boldsymbol{L}_j\boldsymbol{h}_{v,j-1}(t_{i-1}) - \boldsymbol{h}_{v,j}(t_{i-1})] \tag{22b}$$

Multiplying both sides of Eq. (17) by $\bar{\boldsymbol{T}}_j(t_i)$ and utilizing the relationship $\bar{\boldsymbol{T}}_j(t_i)\,\bar{\boldsymbol{f}}_j(t_i) = \boldsymbol{d}_j(t_i) - \bar{\boldsymbol{s}}_j(t_i)$ [Eq. (19)] yields

$$[\boldsymbol{I}_3 + \bar{\boldsymbol{T}}_j(t_i)\,\boldsymbol{P}_j(t_{i-1})]\,\boldsymbol{d}_j(t_i) = \bar{\boldsymbol{T}}_j(t_i)\,\boldsymbol{f}_j(t_i) + \bar{\boldsymbol{s}}_j(t_i) + \bar{\boldsymbol{T}}_j(t_i)\,\boldsymbol{q}_j(t_{i-1}) \tag{23}$$

Comparing Eq. (23) with Eq. (20), we obtain

$$[\boldsymbol{I}_3 + \bar{\boldsymbol{T}}_j(t_i)\,\boldsymbol{P}_j(t_{i-1})]\,\boldsymbol{T}_j(t_i) = \bar{\boldsymbol{T}}_j(t_i) \tag{24a}$$

$$[\boldsymbol{I}_3 + \bar{\boldsymbol{T}}_j(t_i)\,\boldsymbol{P}_j(t_{i-1})]\,\boldsymbol{s}_j(t_i) = \bar{\boldsymbol{s}}_j(t_i) + \bar{\boldsymbol{T}}_j(t_i)\,\boldsymbol{q}_j(t_{i-1}) \tag{24b}$$

where $\boldsymbol{I}_3$ is a 3×3 unit matrix. We call Eqs. (22a), (22b) and (24a), (24b) "field transmission rule" and "point transmission rule", respectively. Supposing that the dynamic influence coefficient matrix and additional vector of the right-hand side of node $j-1$, $\boldsymbol{T}_{j-1}(t_i)$ and $\boldsymbol{s}_{j-1}(t_i)$, are known, the ones of node j, that is $\boldsymbol{T}_j(t_i)$ and $\boldsymbol{s}_j(t_i)$, are obtained through the field and point transmission rules Eqs. (22a), (22b) and (24a), (24b). In other words, if the dynamic influence coefficient matrix and additional vector of node 0 are known, the ones of other nodes are successively computed from node 1 to node n because the field and point transmission rules represent a recurrent formula to yield $\boldsymbol{T}_j(t_i)$ and $\boldsymbol{s}_j(t_i)$. Since the root of the probe, node 0, is assumed to have no relative movement with respect to the unstretched probe, the displacement and force vectors at node 0 are regarded as $\boldsymbol{d}_0(t_i) = 0$ and $\boldsymbol{f}_0(t_i) \neq 0$. Substituting the $\boldsymbol{d}_0(t_i)$ and the $\boldsymbol{f}_0(t_i)$ into Eq. (20) with subscript $j = 0$, we obtain the dynamic influence coefficient matrix and additional vector of node 0.

$$\boldsymbol{T}_0(t_i) = \boldsymbol{0}_3, \quad \boldsymbol{s}_0(t_i) = \boldsymbol{0} \tag{25}$$

where $\boldsymbol{0}_3$ is a 3×3 zero matrix.

Node j slantingly connects with the jth and (j+1)th beam elements as shown in Fig. 7. Therefore, coordinate transform is necessary through the point transmission rule. The transform of coordinate from jth beam element to node j is operated as:

$$\boldsymbol{\Phi}\,\bar{\boldsymbol{T}}_j(t_i)\,\boldsymbol{\Phi}^{\mathrm{T}} \Rightarrow \bar{\boldsymbol{T}}_j(t_i), \quad \boldsymbol{\Phi}\,\bar{\boldsymbol{s}}_j(t_i) \Rightarrow \bar{\boldsymbol{s}}_j(t_i), \quad \boldsymbol{\Phi} = \begin{bmatrix} \cos\varphi & -\sin\varphi & 0 \\ \sin\varphi & \cos\varphi & 0 \\ 0 & 0 & 1 \end{bmatrix} \tag{26a}$$

The transform of coordinate from node j to (j+1)th beam element is operated as:

$$\boldsymbol{\Phi}\,\boldsymbol{T}_j(t_i)\,\boldsymbol{\Phi}^{\mathrm{T}} \Rightarrow \boldsymbol{T}_j(t_i), \quad \boldsymbol{\Phi}\,\boldsymbol{s}_j(t_i) \Rightarrow \boldsymbol{s}_j(t_i) \tag{26b}$$

The dynamic influence coefficient matrix $\boldsymbol{T}_j(t_i)$ and additional vector $\boldsymbol{s}_j(t_i)$ are successively computed from node 0 to node n through Eqs. (22a), (22b), (24a)–(26b).

The right-hand side of the system (top of the probe) is free, it follows that the force vector at the right-hand side of node n is zero, that is $\boldsymbol{f}_n(t_i) = \boldsymbol{0}$. Substituting $\boldsymbol{f}_n(t_i) = \boldsymbol{0}$ into Eq. (20), we obtain the displacement vector of node n as:

$$\boldsymbol{d}_n(t_i) = \boldsymbol{s}_n(t_i) \tag{27}$$

Displacement vectors of other nodes are recursively obtained from node $n-1$ to node 0 by applying the following equations, which are derived from Eqs. (17), (6) and (20).

$$\begin{aligned} &\bar{\boldsymbol{f}}_j(t_i)=\boldsymbol{q}_j(t_{i-1})+\boldsymbol{f}_j(t_i)-\boldsymbol{P}_j(t_{i-1})\boldsymbol{d}_j(t_i), \quad \boldsymbol{f}_{j-1}(t_i)=\boldsymbol{L}_j\,\bar{\boldsymbol{f}}_j(t_i) \\ &\boldsymbol{d}_{j-1}(t_i)=\boldsymbol{T}_{j-1}(t_i)\,\boldsymbol{f}_{j-1}(t_i)+\boldsymbol{s}_{j-1}(t_i) \end{aligned} \tag{28}$$

where $j: n \rightarrow 1$. The following coordinate transform is also necessary for $\bar{\boldsymbol{f}}_j(t_i)$ and $\boldsymbol{f}_{j-1}(t_i)$ in the process of Eq. (28) because of the slanting connection of jth beam element with node $j-1$ and node j.

$$\boldsymbol{\Phi}^{\mathrm{T}}\bar{\boldsymbol{f}}_j(t_i) \Rightarrow \bar{\boldsymbol{f}}_j(t_i), \quad \boldsymbol{\Phi}^{\mathrm{T}}\boldsymbol{f}_{j-1}(t_i) \Rightarrow \boldsymbol{f}_{j-1}(t_i) \tag{29}$$

Velocity and acceleration vectors $\dot{\boldsymbol{d}}_j(t_i)$ and $\ddot{\boldsymbol{d}}_j(t_i)$ are given by Eq. (16) after the computation of displacement vectors $\boldsymbol{d}_j(t_i)$.

4. Numerical computations

4.1 Reproduction of the experimental results

Numerical simulations were implemented by using the analytical model obtained in Section 2. A standard computer (CPU 2.4 GHz, 512MB RAM) was used in the computation. The compiler was Fortran 95 and double precision variables were used. The Newmark-β method ($\beta = 1/4$, $\gamma = 1/2$) was employed as a step-by-step time integration scheme. We confirmed

d_h	: Diameter of helical tube	1.2 m
d_{in}	: Inner diameter of heating tube	24.2 mm
u	: Feed speed of probe	200 mm/s
ρ_f	: Air-flow density	1.023 kg/m^3
Q	: Supply rate of air-flow	63.0 m^3/h
d_c	: Diameter of cable	8.35 mm
l	: Length of carrier cable	10, 20, 30, 40, 50 m
l_G	: Length of guide cable	2.5 m
ρ_c	: Density of probe	0.111 kg/m
(EA)	:Tensile rigidity of cable	1.1×10^5N
(EI)	: Flexural rigidity of cable	4.8×10^{-2} Nm^2
d_f	: Diameter of float	19.0 mm
p_f	: Float pitch	100 mm
$\hat{k}$	: Contact rigidity between float and tube	10^5 N/m
μ	: Coefficient of kinetic friction	0.15
δ	: Coefficient of proportional viscous damping	5.0×10^{-5} s

Table 2. Parameters of numerical simulation

that the results by the Wilson-θ method (θ = 1.4) were almost the same as the ones by the Newmark-β method.

Parameters of the numerical simulation are listed in Table 2. Since probes of constant length are treated, five probes with different length are provided for numerical simulation. The five

probes are different in length of carrier cable, l = 10, 20, 30, 40 and 50m as listed in Table 2. The total length of the cable L is the length of carrier cable l plus that of guide cable l_G = 2.5 m. As mentioned in Section 2.2 (b), numerical simulation of the probe is approximately regarded as a momentary situation in which the inserted length of the probe into the helical part of the heating tube reaches L. An initial condition was assumed to be static. The drag force of Eq. (10) simultaneously began to act on the all floats at the beginning of the simulation. At the same time, the probe began to move at a feeding speed u. Time step size Δt = 0.0001 s was chosen for the step-by-step integration and time historical responses during t = 0 – 8 s were computed. The numerical simulations were impossible because of a numerical divergence when the time step size was larger than 0.0001 s in both the Newmark-β and the Wilson-θ methods.

Displacements of the node corresponding to the sensor are shown in Fig. 11. Axial displacement $x_j(t)$ and radial displacement $y_j(t)$ are shown in Fig. 11(a and b), respectively. The vibration of the probe increases as the length of probe become longer. Particularly, the radial displacement rapidly increases between l = 30 and 40 m. Since the vibration of probe in experiment rapidly increased after the sensor passed through the middle point of the helical part (see Fig. 4), the results of the numerical simulation agree with the experimental results.

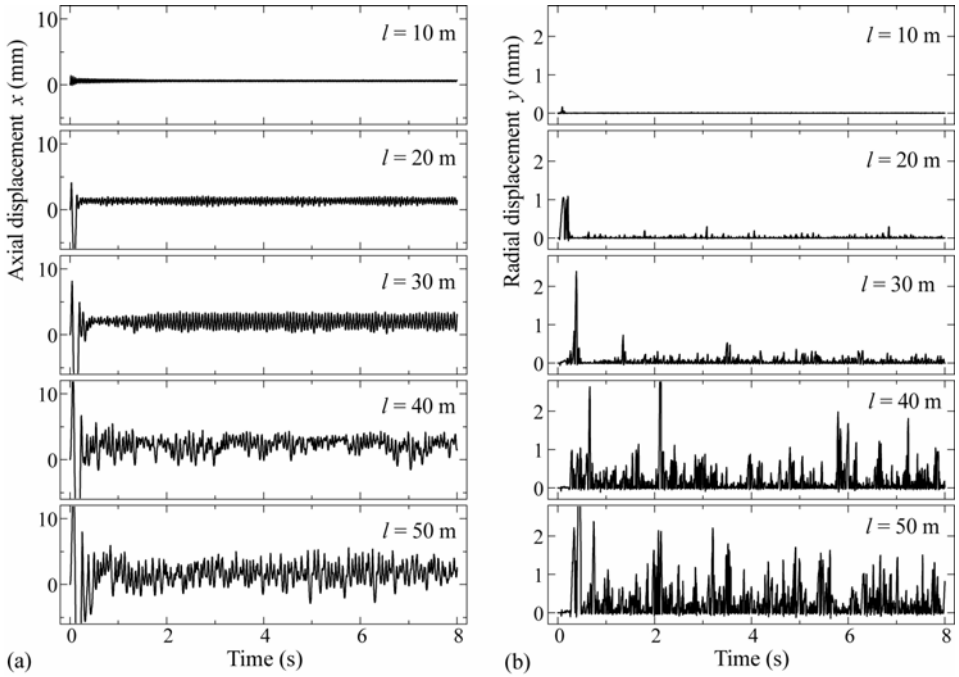

Fig. 11. Vibration of probe in insertion process: (a) axial and (b) radial displacements.

Finally, the inserted length of the probe into the helical heating tube reaches 55–60 m. Magnifications of the axial and the radial vibrations of l = 55 m (total length $L = l + l_G$ (2.5m) = 57.5 m) are shown in Fig. 12(a and b). Other parameters were the same as the ones listed in Table 2. The vibrations during t = 1.0–2.5 s are plotted. It is confirmed that the axial and the

radial vibrations are weakly coupled. The locus of the vibration is plotted in Fig. 13(a). The horizontal axis indicates a fixed coordinate along the inner wall of the heating tube and the vertical axis shows the radial displacement. The probe is leaping around and shows an inchworm-like motion. The motion of the sensor in the experiment, where the inserted length of the probe into the helical part was about 57 m, is shown in Fig. 13(b). It was given by a tracing of the images of sensor, which was taken by a high-speed camera. Although both the axial and the radial motions in the experiment are larger than that of the simulation, the result of the simulation qualitatively agrees with the one of the experiment. The Fourier analysis of the axial and the radial vibrations of L = 57.5 m are shown in Fig. 14(a and b), respectively. The vibrations during t = 0.5–4.5 s, which are free from the transient response, are provided to the Fourier analysis. It is confirmed that the axial and the radial vibrations are coupled since an identical peak of 14 Hz appears in both vibrations. The frequency of the coupled vibration in the experiment was about 20 Hz, as mentioned in Section 2.1 c. There is a discrepancy between the experiment and the numerical simulation in this point. However, the results of numerical simulations are qualitatively similar to the ones of the experiment.

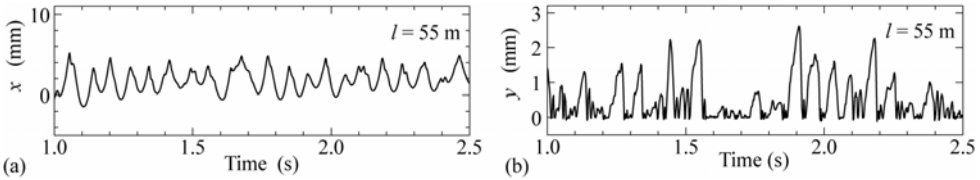

Fig. 12. Vibration of probe; l = 55 m, t = 1.0–2.5 s: (a) axial and (b) radial displacements.

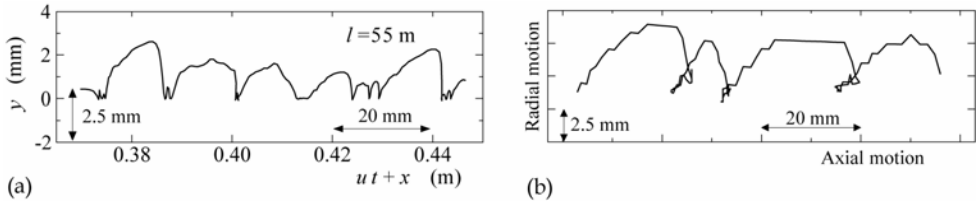

Fig. 13. Locus of probe; (a) numerical simulation of l=55 m, t=1.8–2.2 s and (b) in experiment, inserted length around 57 m.

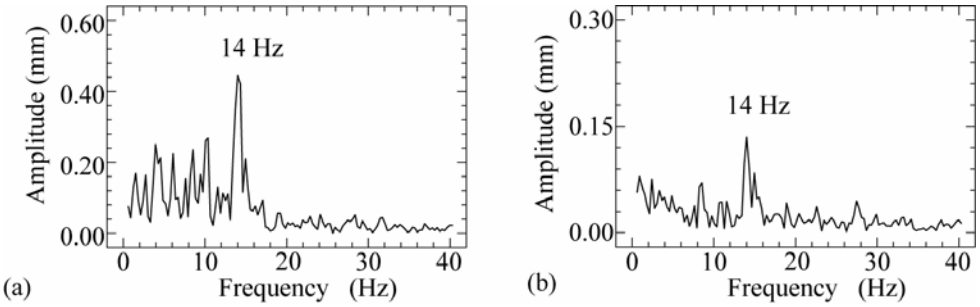

Fig. 14. Frequency analysis of vibration; l = 55m : (a) axial and (b) radial displacements.

A numerical simulation of the probe without feeding (feeding speed u = 0 mm/s) was implemented. The length of carrier cable was l = 50 m, which showed a severe vibration with feeding speed u = 200 mm/s as shown in Fig. 11. Other parameters were the same as the ones listed in Table 2. This simulation corresponds to the experiment that the dry compressed air streamed in the heating tube but the probe was not fed as mentioned in Section 2.1 d. Displacements of the node corresponding to the sensor are shown in Fig. 15. Both the axial and the radial displacements converged at constant values at an initial transient response. This result is similar to the experiment. It follows that the experimental result without feeding is also supported by the numerical simulation.

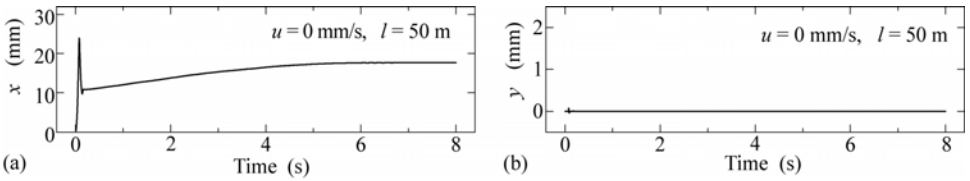

Fig. 15. Response at u = 0 mm/s; l = 50m : (a) axial and (b) radial displacements.

More numerical simulations were implemented in order to enhance the validity of the analytical model. Numerical simulations with variation of feeding speed, diameter of the helix and air supply rate were implemented. Only one parameter (feeding speed, diameter of the helix or air supply rate) was changed, and the other parameters were the same as Table 2. The length of carrier cable was l = 50 m as well as the simulation of the non-feeding probe, Fig. 15. The simulations of feeding speed u = 100 and 400 mm/s, diameter of the helix d_h = 2.5 m and air supply rate Q = 40m^3/h are shown in Figs. 16–18, respectively. In Fig. 16,the vibration of the probe became small at low feeding speed u = 100 mm/s, but large at high feeding speed u = 400 mm/s, compared with the result of l = 50 m in Fig. 11 (u = 200 mm/s). The vibration also became small in the case of large helical diameter (Fig. 17) and low supply rate of the air flow (Fig. 18). These results are similar to the experiments mentioned in Section 2.1 f. Note that in the case of Q = 40m^3/h, an ability to insert the actual probe is not guaranteed for lack of a drag force (Inoue et al., 2007).

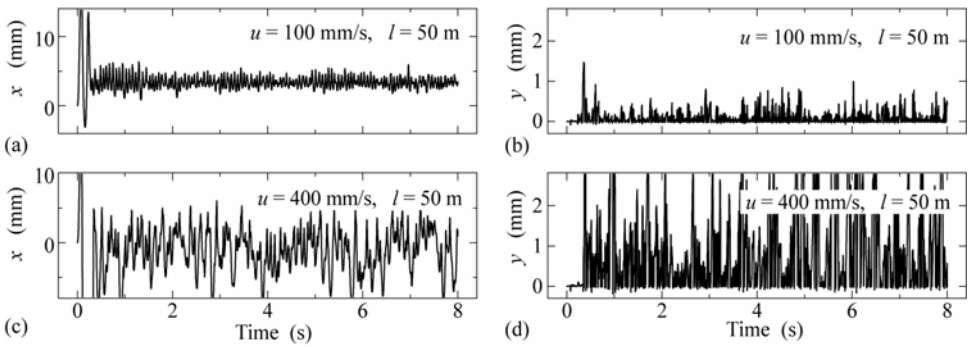

Fig. 16. Vibration of probe; l = 50m: (a) axial and (b) radial displacements at feeding speed u = 100 mm/s, (c) axial and (d) radial displacements at u = 400 mm/s.

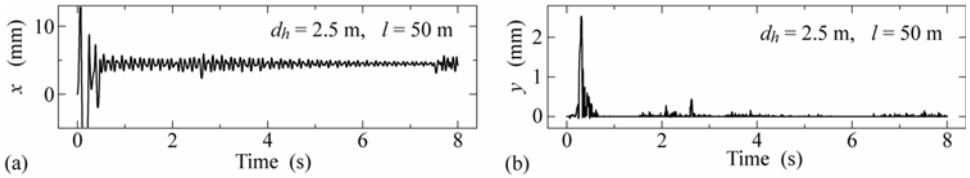

Fig. 17. Vibration of probe; diameter of helix d_h = 2.5 m, l = 50m: (a) axial and (b) radial displacements.

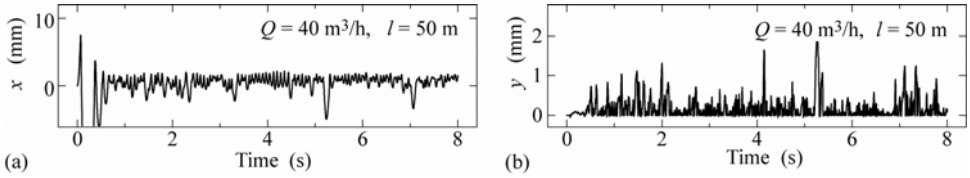

Fig. 18. Vibration of probe; air supply rate Q = 40 m³/h, l = 50 m: (a) axial and (b) radial displacements.

The numerical simulation was qualitatively able to reproduce the experimental results. Thus, the validity of the analytical model obtained in this study was confirmed through the numerical simulations. It was demonstrated that the vibration of probe was caused by Coulomb friction between the floats and the inner wall of the heating tube.

4.2 Entire behavior of probe

A numerical simulation of the insertion process to the length of carrier cable l = 55 m is implemented, and the entire probe behavior is shown in Fig. 19. The other parameters are the same as the ones in Table 2. The total length of the cable is $L = l$ (55 m) + l_G (2.5 m) = 57.5 m. Momentary shapes of the entire probe during 1.56–1.65 s are displayed at an interval of 0.01 s. Axial and radial displacements are shown in Fig. 19(a and b), respectively. Each of the horizontal axes in Fig. 19(a and b) indicates a distance from the entrance of the helical heating tube. It is a fixed coordinate along the helical heating tube. The root of the probe, which is supposed to be located at the entrance of the helical heating tube, corresponds to L = 0 m, and the top of the cable is situated at L = 57.5 m. The vertical axes in Fig. 19(a) indicate the axial displacements, and the ones in Fig. 19(b) indicate the radial displacements. Although the direction of the axial displacement in the ordinate of Fig. 19(a) is the same as the coordinate along the heating tube L, it is displayed at right angles with the coordinate L. The sensor position is indicated as broken lines both in Fig. 19(a and b). The following characteristics are found in Fig. 19.

a. A shaded area in Fig. 19(a) indicates a segment in which a gradient of the axial displacement along the heating tube (dx/dL) obviously shows a negative value. The identical areas are also shaded in Fig. 19(b). We are able to observe a radial displacement in the shaded area. Furthermore, it becomes larger as the negative gradient of the axial displacement ($dx/dL < 0$) becomes steeper.
b. Local maxima of the axial displacement, points "A" and "B" in Fig. 19(a), move toward the top of the probe as the time step goes forward. This is a wave-like motion rather than a vibration. A reflection of the wave is not clearly observed in Fig. 19(a and b). It

seems that the noticeable peak at 14 Hz in Fig. 14 signifies the frequency of repetitiveness of the wave-like motion.

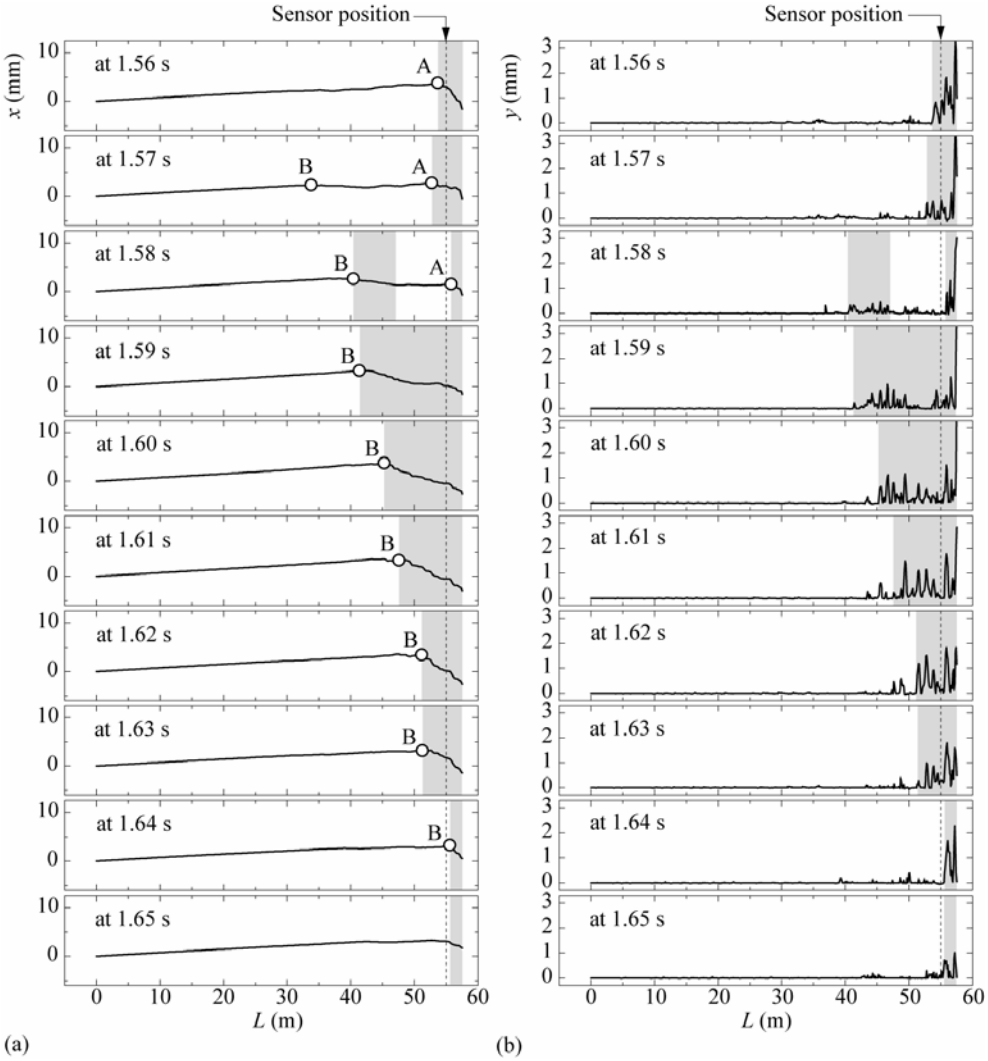

Fig. 19. Entire behavior of probe in the insertion process: (a) axial and (b) radial displacements.

c. Large amplitudes in the radial displacement are limited in the area near the top of the cable.

The countermeasures against vibration, which include a long guide cable and a large float of guide cable, were devised in order to reduce the RF sensor noise. It was confirmed that the countermeasures are effective in suppressing the vibration in the experiments. Although the countermeasures were empirically obtained, the entire behavior of the probe shown in Fig. 19 implies the mechanism of the countermeasures as follows:

a. The amplitude in the radial displacement is small at a position away from the top of the cable as shown in Fig. 19(b). The long guide cable keeps the sensor part away from the top of the cable, and the radial (displacement) vibration at the sensor position becomes small. Since the RF sensor noise is highly correlated to the radial vibration, it is reduced by means of the long guide cable. This effect has been also confirmed in the experiments (Inoue et al., 2007a).
b. In the shaded area in Fig. 19, where the gradient $dx/dL<0$, the driving force (drag force) acting on the probe is smaller than that of the non-shaded area. Originally, a tensile force acts on the probe in the insertion process. However, a "compressive force" is generated in the shaded area because of the lack of driving force, and the shaded area is pushed from the backward non-shaded area. Consequently, a kind of buckling happens and the probe in the shaded area, which is supposed to move in contact with the inside of the helical tube, rises off the inner wall of the heating tube. This phenomenon travels toward the top of the cable and makes the wave-like motion. At a fixed point, for example the sensor position, it appears as a vibration. This is the mechanism of the probe vibration. Similar rising (lift-off) phenomena were reported in previous studies (Bihan, 2002; Giguere et al., 2001; Tian and Sophian, 2005), but significant vibration was not reported in these studies. Relatively severe vibration induced by this rising phenomenon is a peculiar characteristic of this study. Since the shaded area is generated in the forward section of the probe, the large float of guide cable makes the driving force acting on the forward section large, and it reduces the "compressive force" acting on the shaded area. As a result, the large float of guide cable works to suppress the vibration at the sensor part.

4.3 Improvement of the countermeasure

The empirical countermeasures to suppress the vibration at the sensor part are supported by the numerical simulations. On the basis of the mechanism which suppresses the vibration, the following improvements are suggested:

a. Use of a longer guide cable. This acts on the principle that the vibration becomes smaller as the length between the sensor position and the top of cable becomes longer.
b. Further increase of the driving force of the guide cable. This makes the "compressive force" acting on the forward section of the probe relatively weak, and prevents the probe from rising off the inner wall of the heating tube.
c. Decrease the driving force of the carrier cable. This is similar to suggestion b. It directly reduces the "compressive force" toward the forward section of the probe by reducing the driving force of the backward section.

In reference to suggestion a, it makes the probe length inserted into the heating tube longer. Since the steam generator of the "Monju" has 140-layered heating tubes, use of an excessively long guide cable would negatively affect maintenance efficiency. Thus, a guide cable longer than 10m is undesirable in actual use. Suggestions b and c involve control of the drag force acting on the floats. There are two means to vary the drag force: One is to alter the float size, where the float is spherical. The other is to replace the float shape. However, it is difficult to practicably use a non-spherical float as it would compromise the smooth passage of the probe. Hence, control of the drag force by alteration of the float size is considered here.

The inner diameter of the heating tube is 24.2 mm, and some points are smaller than 24.2mm because of projections caused by welding. Consequently, a float diameter of 20 mm, which has been utilized in the countermeasure, seems to be the upper limit since a larger float would probably clog the heating tube. Thus, only suggestion c is adopted. The probe is fed into the upper side of the steam generator (see Fig. 1), goes down the heating tube, passes the helical part, goes up the straight part and reaches the upper side again. A strong driving force is needed when the probe passes the helical part and goes up the straight part of heating tubes. Thus, there is also a minimum float diameter in order to guarantee the driving force needed to propel the probe to achieve the inspection of the heating tubes. We choose the diameter for the float attached to carrier cable d_f = 16 mm.

The numerical simulation with these improvements, where the length of guide cable l_G = 10 m, the diameter of the float attached to guide cable d_f = 20 mm and the one to carrier cable d_f = 16 mm, is implemented. The length of carrier cable l = 50 m, (total length L is 60 m) and the other parameters are the same as the ones in Table 2. The vibration at the sensor part is shown in Fig. 20. Suppression of the vibration at the sensor part is almost accomplished in the radial direction. Comparing this result with the one of l = 50 m in Fig. 11, the validity of this improvement is indisputable. We can assess that the performance of the improved probe is satisfactory to suppressing the vibration.

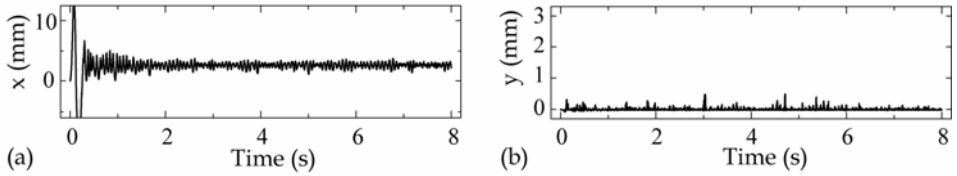

Fig. 20. Vibration of probe in the insertion process with the proposed improvement, diameter of the float attached to the guide cable 20 mm, carrier cable 16mm and length of the guide cable l_G = 10 m : (a) axial and (b) radial displacements.

In 2010, the fast breeder reactor "Monju" in Japan resumed work after a long time tie-up of operation. The tie-up was cause by a leakage accident of sodium in a heat exchanging system. The resumption of "Monju" was the target of public attention. An improved probe based on this study practically come into service for the defect detection of heating helical tubes installed in "Monju". A reliable inspection is performed and it has kept a safe operation of "Monju".

5. Conclusions

A defect detection of a helical heating tube installed in a fast breeder reactor "Monju" in Japan is operated by a feeding of an eddy current testing probe. A problem that the eddy current testing probe vibrates in the helical heating tubes happened and it makes the detection of defect difficult. In this study, the cause of the vibration of the eddy current testing probe was investigated. The results are summarized as follows:

a. The cause of the vibration was assumed to be Coulomb friction and an analytical model of the vibration incorporating Coulomb friction was obtained.
b. An effectual algorithm for the numerical simulation of the eddy current testing probe was formulated by applying the Transfer Influence Coefficient Method to the equation of motion derived from the analytical model.

c. The results of numerical simulations qualitatively reproduced the several characteristics of the vibration of the eddy current testing probe, which were obtained by experiments. The validity of the assumption that the vibration is cause by Coulomb friction was confirmed by an agreement between the results of experiments and numerical simulations.
d. The probe's motion in its entirety under the vibration conditions was obtained by the numerical simulation. The mechanism of the vibration and the countermeasures were revealed through a discussion on the probe's entire motion.
e. An improvement of the countermeasure was proposed based on the probe's entire motion. The validity of the proposed improvement was demonstrated through a numerical simulation. The improvement was effective both in the insertion and the return processes.

6. Acknowledgements

This investigation was performed through collaboration between Kyushu University and Japan Atomic Energy Agency (JAEA) as public research of Japan Nuclear Cycle. Here the authors would like to acknowledge the authorities concerned.

7. References

Belytschko, T. & Hughes, T.J.R. (1983). *Computational methods for transient analysis*, Belytschko, T. & Bathe, K.J. (Eds.), Computational Methods in Mechanics, Vol. 1, (417–471), Elsevier Science Publishers B.V., ISBN 0444864792, Amsterdam.

Bihan, Y.L. (2002). Lift-off and tilt effects on eddy current sensor measurements: a 3-D finite element study. *Eur. Phys. J. Appl. Phys.*, Vol. 17, (25–28), ISSN 0021-8979.

Crisfield, M.A. & Shi, J. (1996). An energy conserving co-rotation procedure for non-linear dynamics with finite elements. *Nonlinear Dyn.*, Vol. 9, (37–52), ISSN 1090-0578.

Giguere, S.; Lepine, B. & Dubois, J.M.S. (2001). Pulsed eddy current technology: characterizing material loss with gap and lift-off variations. *Res. Nondestructive Eval.*, Vol. 13, (119–129), ISSN 1075-4862.

Inoue, T.; Sueoka, A.; Nakano, Y.; Kanemoto, H.; Imai, Y. & Yamaguchi, T. (2007). Vibrations of probe used for the defect detection of helical heating tubes in a fast breeder reactor. Part 1. Experimental results by using mock-up. *Nucl. Eng. Des.*, Vol. 237, (858–867), ISSN 0029-5493.

Inoue, T.; Sueoka, A. & Shimokawa, Y. (1997). Time historical response analysis by applying the Transfer Influence Coefficient Method, *Proceedings of the Asia-Pacific Vibration Conference '97*, Vol. 1, pp. 471–476, Kyongju (Korea), November 1997.

Isobe, M.; Iwata, R. & Nishikawa, M. (1995). *High sensitive remote field eddy current testing by using dual exciting coils*, Collins, R.; Dover, W.D.; Bowler, J.R. & Miya, K. (Eds.), Nondestructive Testing Mater. (Studies in Applied Electromagnetics and Mechanics), Vol. 8, (145–152). IOS Press, ISBN 9051992394, Amsterdam.

Kondou, T.; Sueoka, A.; Moon, D.H.; Tamura, H. & Kawamura, T. (1989). Free vibration analysis of a distributed flexural vibrational system by the Transfer Influence Coefficient Method. *Theor. Appl. Mech.*, Vol.37, (289–304), ISSN 0285-6024.

Pestel, E.C. & Leckie, F.A. (1963). *Matrix Methods in Elastomechanics*, McGraw-Hill Publishers, ISBN 0070495203, New York.

Robinson, D. (1998). Identification and sizing of defects in metallic pipes by remote field eddy current inspection. *Tunnel. Underground Space Technol*, Vol. 13, (17–27), ISSN 0886-7798.

Sueoka, A.; Tamura, H.; Ayabe, T. & Kondou, T. (1985). A method of high speed structural analysis using a personal computer. *Bull. JSME*, Vol. 28, (924–930), ISSN 1344-7653.

Tian, G.Y. & Sophian, A. (2005). Reduction of lift-off effects for pulsed eddy current NDT. *NDT&E Int.*, Vol. 38, (319–324), ISSN 0963-8695.

Xie, Y.M. (1996). An assessment of time integration schemes for non-linear dynamic equations. *J. Sound Vibrat.*, Vol. 192, (321–331), ISSN 0022-460X.

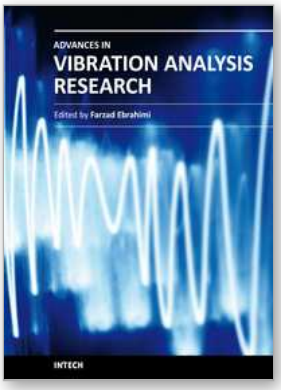

Advances in Vibration Analysis Research

Edited by Dr. Farzad Ebrahimi

ISBN 978-953-307-209-8
Hard cover, 456 pages
Publisher InTech
Published online 04, April, 2011
Published in print edition April, 2011

Vibrations are extremely important in all areas of human activities, for all sciences, technologies and industrial applications. Sometimes these Vibrations are useful but other times they are undesirable. In any case, understanding and analysis of vibrations are crucial. This book reports on the state of the art research and development findings on this very broad matter through 22 original and innovative research studies exhibiting various investigation directions. The present book is a result of contributions of experts from international scientific community working in different aspects of vibration analysis. The text is addressed not only to researchers, but also to professional engineers, students and other experts in a variety of disciplines, both academic and industrial seeking to gain a better understanding of what has been done in the field recently, and what kind of open problems are in this area.

INTECH
open science | open minds

InTech Europe
University Campus STeP Ri
Slavka Krautzeka 83/A
51000 Rijeka, Croatia
Phone: +385 (51) 770 447
Fax: +385 (51) 686 166
www.intechopen.com

InTech China
Unit 405, Office Block, Hotel Equatorial Shanghai
No.65, Yan An Road (West), Shanghai, 200040, China
中国上海市延安西路65号上海国际贵都大饭店办公楼405单元
Phone: +86-21-62489820
Fax: +86-21-62489821